

<https://doi.org/10.1038/s41698-025-00897-7>

Multimodal spatial proteomic profiling in acute myeloid leukemia

Check for updates

Christopher P. Ly^{1,8}, Ivo Veletic^{1,8}, Christopher D. Pacheco¹, Enes Dasdemir^{1,2}, Fatima Z. Jelloul³, Sammy Ferri-Borgogno⁴, Akshay V. Basi¹, Javier A. Gomez¹, Jessica L. Root¹, Patrick K. Reville¹, Sonali Jindal⁵, Sreyashi Basu⁵, Padmanee Sharma⁵, Andres E. Quesada³, Carlos Bueso-Ramos³, Taghi Manshouri¹, Branko Cuglievan⁶, Miriam Garcia⁶, Jared K. Burks¹ ✉ & Hussein A. Abbas^{1,7} ✉

Acute myeloid leukemia (AML) resides in an immune-rich microenvironment, yet, immune-based therapies have faltered in eliciting durable responses. Bridging this paradox requires a comprehensive understanding of leukemic interactions within the bone marrow microenvironment. We optimized a high-throughput tissue-microarray-based pipeline for high-plex spatial immunofluorescence and mass cytometry imaging on a single slide, capturing immune, tumor, and structural components. Using unbiased clustering on the spatial K function, we unveiled the presence of tertiary lymphoid-like aggregates in bone marrow, which we validated using spatial transcriptomics and an independent proteomics approach. We then found validated TLS signatures predictive of outcomes in AML using an integrated public 480-patient transcriptomic dataset. By harnessing high-plex spatial proteomics, we open the possibility of discovering novel structures and interactions that underpin leukemic immune response. Further, our study's methodologies and resources can be adapted for other bone marrow diseases where decalcification and autofluorescence present challenges.

Acute myeloid leukemia (AML) is a malignant clonal disorder of the hematopoietic system¹. Approximately 50% of patients achieve complete remission with induction therapy, but overall survival remains <30% at five years. Further, AML patients who relapse or are refractory to chemotherapy have a dismal prognosis². Immunotherapies have emerged as a promising therapeutic option in solid cancers, yet efficacy in AML has been disappointing in clinical trials³.

Leukemic cells have been shown to reprogram the surrounding bone marrow microenvironment (BMM) in the course of disease progression, modulating anti-tumor immune response and enabling immune evasion^{4,5}. Filling the AML-immune cell interaction knowledge gap to uncover actionable therapeutics requires deeper insights into how cells within the BMM interact. The advent of high-parameter targeted spatial proteomics technologies^{6–9}, which capture the spatial distribution of proteins and their expression, has allowed for a richer understanding of the tumor immune microenvironment. Non-spatial technologies such as single-cell RNA

sequencing and flow cytometry disaggregate cells and are unable to resolve tissue structure, discarding critical organization of cell interactions such as tertiary lymphoid structures (TLS) which, as part of the adaptive immune response, have been shown to have prognostic implications in cancer through improved response to immune checkpoint therapy¹⁰ and increased lymphocyte infiltration¹¹.

Sequential immunofluorescence (IF) is a novel technology that allows for the high-plex interrogation of the spatial proteome. However, the technique comes with unique challenges in formalin-fixed, paraffin-embedded (FFPE) bone marrow tissue: endogenous autofluorescence, tissue and bone deformation through repeated cycles of imaging, and the necessity of decalcification, which degrades morphology and immunoreactivity¹².

Given these limitations, we developed a robust sample-to-analysis workflow to spatially capture the proteome of the BMM using an integrative combination of IF and imaging mass cytometry (IMC), maximizing the

¹Department of Leukemia, The University of Texas MD Anderson Cancer Center, Houston, TX, USA. ²Department of Biology and Biochemistry, University of Houston, Houston, TX, USA. ³Department of Hematopathology, The University of Texas MD Anderson Cancer Center, Houston, TX, USA. ⁴Department of Gynecologic Oncology and Reproductive Medicine, The University of Texas MD Anderson Cancer Center, Houston, TX, USA. ⁵Department of Immunology, The University of Texas MD Anderson Cancer Center, Houston, TX, USA. ⁶Department of Pediatrics, The University of Texas MD Anderson Cancer Center, Houston, TX, USA. ⁷Department of Genomic Medicine, The University of Texas MD Anderson Cancer Center, Houston, TX, USA. ⁸These authors contributed equally: Christopher P. Ly, Ivo Veletic. ✉ e-mail: jburks@mdanderson.org; habbas@mdanderson.org

strengths of each modality and enabling spatial alignment at the single-cell level. Additionally, hematoxylin and eosin (H&E) staining on an adjacent slide captures structural components, granting a comprehensive view of the BMM.

We present an optimized workflow for the high-plex spatial proteomic imaging of leukemic BMM using the COMET sequential IF system to uncover the appearance of a TLS-like aggregate in AML-affected bone marrow and demonstrate the capability for discovering novel AML-BMM interactions with prognostic implications. Furthermore, we provide a resource of validated antibodies for use in bone marrow imaging. These strategies allow high-throughput multimodal spatial characterization and can be applied to other bone marrow diseases beyond AML.

Results

An optimized high-plex spatial proteomics workflow

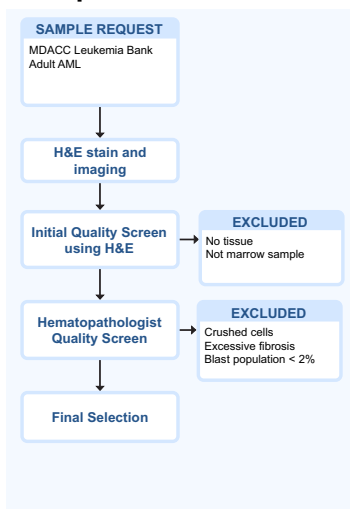
We developed a robust sample-to-analysis workflow optimized for speed, flexibility, and accurate recapitulation of the bone marrow (Fig. 1). Seven bone marrow biopsies from seven adult AML patients were organized into

two TMAs using an automated TMA builder for high-throughput, reduced staining and imaging costs, and reduced batch effect without compromising spatial relationships¹³. Compared to manual TMA generation, the automated TMA builder provided faster turnaround time and consistent spacing, thickness, and core height. We found a 1.5-mm core diameter to be ideal for tissue adhesion as smaller cores (≤ 1 mm) tended to detach under our heat-induced epitope retrieval (HIER) protocol (see Methods). The resulting TMA FFPE block was sectioned, mounted onto three standard glass slides for H&E staining, proteomic imaging using the COMET IF and Hyperion XTⁱ IMC systems, and any additional assays. The block was then archived for future use. Section thickness was optimized at 4 μ m based on the depth of focus of the COMET as well as signal-to-noise ratio for IF in FFPE tissues¹⁴.

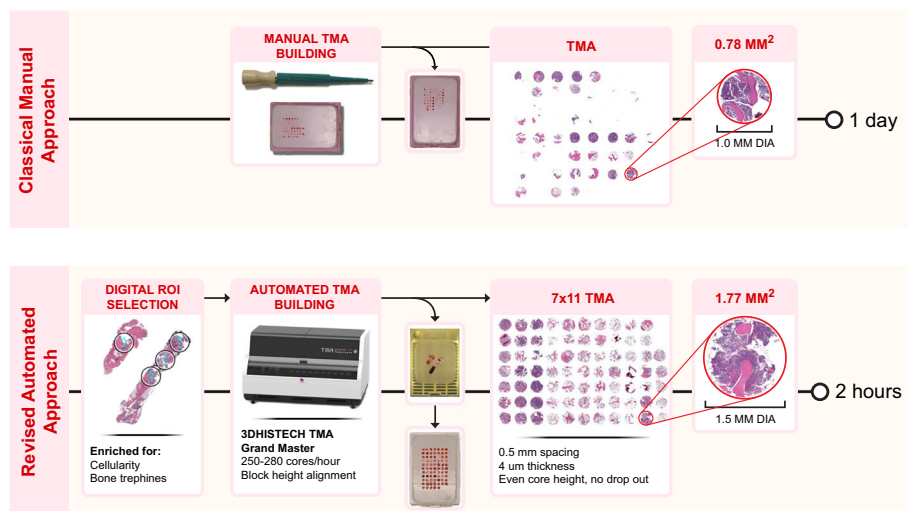
Spatial immunofluorescence in FFPE bone marrow reliably captures the BMM

Using our optimized protocol, we spatially interrogated trephine bone marrows from 7 AML patients (mean age = 67.9 years; range, 62.8–72.55;

Sample Selection



TMA Creation Workflow



Integrative Analytics

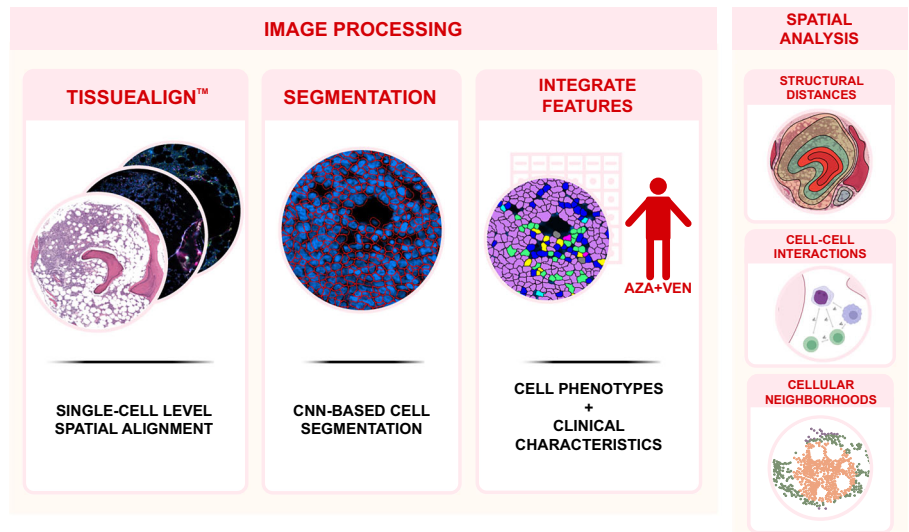
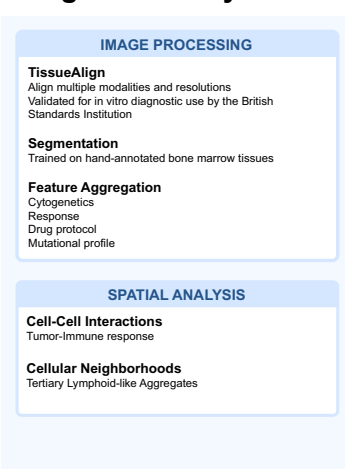


Fig. 1 | Overview of the multimodal bone marrow imaging pipeline. Patient bone marrow biopsies are ordered based on study suitability and then undergo rigorous quality screening. A digital automated approach for TMA building is used, which increases quality, reproducibility, and speed compared to manual TMA building. The analysis workflow begins by aligning all modalities to a common reference.

Imaging data is decomposed into cells by cell segmentation with the U-Net convolutional neural network. Clinical and cell features are aggregated, allowing for comprehensive high-resolution analysis on spatial neighborhoods, structural proximity, and marker enrichment. Figure created in Biorender.

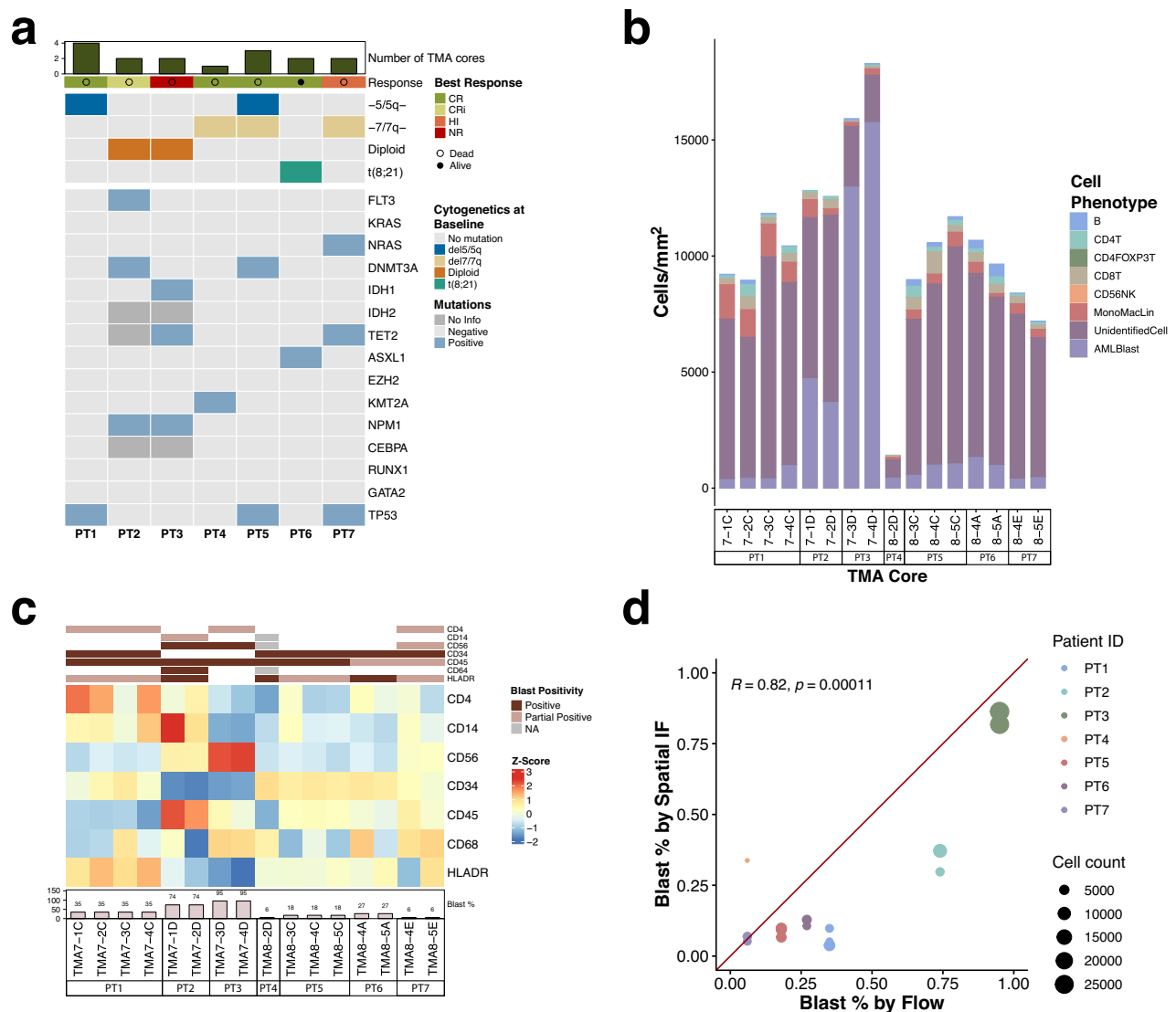


Fig. 2 | Immunofluorescent profiling of the bone marrow corresponds with clinical spectral flow. a Oncoprint of the cytogenetics, response, and mutational characteristics of patients 1–7. **b** Stacked bar plot showing cell type densities by TMA

core. **c** Immunophenotype of AML cells by flow aligns with marker expression in spatial IF. **d** AML blasts measured by IF significantly correlate with reported blast percentages by flow cytometry (Pearson correlation, $R = 0.82$, $p = 0.00011$).

43% male) pre- and post-AML directed therapy (Fig. 2a, characteristics detailed in Table 1, mutational groups Supplementary Fig. 1). This analysis involved 16 TMA cores distributed across two TMAs using the COMET approach. A total of 28 antibodies, which included canonical markers for immune cells ($n = 12$), AML cells ($n = 4$), and functional markers ($n = 12$), were applied to each TMA (Supplementary Table 1). To overcome autofluorescence emerging from lipofuscin, red blood cells, and extracellular matrix components such as collagen and elastin^{15,16}, we devised an algorithm to optimally subtract the autofluorescence from the imaged tissue. Briefly, we utilized the autofluorescence quencher TrueBlack and manually adjusted the magnitude of the subtraction by the average endogenous autofluorescence per cycle to obtain a scaled subtraction effect, which recovered lost signal while minimizing noise (Supplementary Fig. 2a–f).

Out of the segmented 116,488 cells, 63,738 (54.7%) cells had at least one marker that allowed classification/identification (Supplementary Table 2). The remaining cells likely constituted stromal cells, mesenchymal cells, or other immune subsets (such as plasma cells). Protein expression for each cell type is shown in Supplementary Fig. S3a. Cell

types were visualized using dimensionality reduction techniques to identify each cell type (Supplementary Fig. 3b, c). Cell densities for each cell type remained consistent within each patient between cores (Fig. 2b). However, distinct molecular and phenotypic differences emerged across patients with similar disease characteristics. *TP53* mutations were in three out of seven patients and were associated with abnormal karyotype and partial HLA-DR expression. In contrast, both patients with normal karyotype profile exhibited a CD56(+) AML immunophenotype, despite CD56 expression being commonly associated with the t(8;21) translocation¹⁷. Both patients were also the only carriers of the *NPM1* mutation in our cohort. No associations with cytogenetics or other mutational profiles were found. AML immunophenotype was also consistent with expression by flow cytometry (Fig. 2c), and blast percentage significantly correlated ($R = 0.82$, $p = 0.00011$) with flow cytometry done as part of the clinical diagnostic work-up (Fig. 2d). Overall, spatial IF was able to reliably capture cell populations within the BMM of AML patients. These findings suggest that while there is consistency in cellular density within patients, variations in molecular profiles, such as *TP53* mutations

Table 1 | Patient characteristics

Characteristic (unit)	PT1	PT2	PT3	PT4	PT5	PT6	PT7
Demographics							
Age (years)	72	69	68	63	66	62	72
Sex/gender	Male	Female	Male	Male	Female	Female	Female
Race/ethnicity	White	White	White	White	Asian	Hispanic	White
Disease progression							
AML subtype*	AML-M2	AML-M4	AML-M1	AML-M1	AML-M2	AML-M2	AML-M2
Origin	De novo	De novo	t-AML	De novo	t-AML	t-AML	t-AML
Previous malignancies	None	None	RCC, PCa	None	NSCLC, MDS	DLBCL	NHL, BC, HL, MDS
Time since diagnosis (months)	10	0	0	9	7	0	5
Status	Deceased	Deceased	Deceased	Deceased	Deceased	Alive	Deceased
Survival time (months)	17	9	2	11	11	9	9
Cytogenetic and molecular features							
Karyotype	Monosomy 5	Diploid	Diploid	Monosomy 7	Monosomy 5 & 7	t(8;21)	Monosomy 7
Mutations	<i>TP53</i> [†]	<i>NPM1</i> , <i>FLT3</i> , <i>DNMT3A</i> [‡]	<i>NPM1</i> , <i>TET2</i> , <i>IDH1</i> [‡]	<i>KMT2A</i> [‡]	<i>DNMT3A</i> , <i>SH2B3</i> , <i>TP53</i> [‡]	<i>ASXL1</i> [‡]	<i>NRAS</i> , <i>TET2</i> , <i>TP53</i> , <i>SF3B1</i> [‡]
Bone marrow counts							
Cellularity (%)	10–20	95	100	<5	30–40	40	90
Lymphocytes (%)	14	4	2	NA	24	10	36
Blast (%)	35	60	95	6	18	27	6
Peripheral blood counts							
WBC ($\times 10^6$ /L)	NA	41.9	4.98	NA	0.86	0.17	0.99
Lymphocytes (%)	NA	19	10	NA	54	61	78
Monocytes (%)	NA	50	NA	NA	6	5	5
Treatment							
Pre/post treatment	Post	Pre	Pre	Post	Post	Pre	Post
Response category	CR	CRi	NR	CR	CR	CR	HI

AML indicates acute myeloid leukemia, MDS myelodysplastic syndrome, RCC renal cell carcinoma, PCa prostate cancer, NSCLC non-small cell lung cancer, DLBCL diffuse large B-cell lymphoma, NHL Non-Hodgkin's lymphoma, BC breast cancer, HL Hodgkin's lymphoma, IDA idarubicin, CLAD cladribine, LDAC low-dose cytarabine, VEN Venetoclax, DEX dexamethasone, VIN vincristine, AZA azacytidine, IND investigational new drug, CR complete remission, CRi complete remission with incomplete count recovery, NR no response, HI hematologic improvement, NA not available.

*AML subtypes were determined according to the World Health Organization's 5th edition⁶⁸.

[†]Mutations were detected using the 81-gene next-generation sequencing panel, EndLeukemia Assay v1.

[‡]Mutations were detected using the 28-gene next-generation sequencing panel, CMS28.

and karyotypic abnormalities, may influence immunophenotypic features across patients with comparable disease presentations.

Non-destructive sequential IF allows for proteomic validation using the same slide

To further explore other modalities to guide in the identification of the AML-immune microenvironment, we applied spatial IMC, which uses metal-labeled tagged proteins to avoid spectral overlap and image multiple analytes simultaneously. We applied a panel of 25 markers (Supplementary Table 3) on the same slide that we previously performed IF imaging, taking advantage of the non-destructive nature of the COMET to expand the panel and validate the findings of the COMET.

We first tested whether imaging the tissue with sequential IF would degrade IMC staining. We selected two of the previously COMET-imaged TMA cores (TMA7-3C and TMA7-4C) and compared the staining when subsequently imaged on the same slide using IMC. Antibody staining was highly comparable, and markers targeting the same antigen colocalized well, showcasing retained antigenicity and robustness of alignment (Fig. 3a). Correlation analysis showed markers with high signal to background such as CD163, CD34, and Ki67 tended to cluster closely together with their imaging counterpart, as well markers with expected colocalization such as CD3, CD8, and CD45 (Fig. 3b). Nuclear staining showed some degradation

between modalities and affected cell segmentation, leading us to use the 4',6-diamidino-2-phenylindole (DAPI) staining for nuclear segmentation going forward (Supplementary Fig. 4a, b).

To further evaluate IF to IMC performance, we separately phenotyped the cells iteratively captured from IF and IMC to compare how cell assignment differed (Supplementary Table 4). Canonical markers retained expected expression across cell types in both modalities (Supplementary Fig. 4a). Identities of CD34(+) blasts, and CD8(+) and CD4(+) T cells were generally concordant, with IMC displaying higher specificity (82%, 79%, and 71% concordance of IMC positive populations with IF, respectively) than IF (60%, 52%, and 40% concordance) (Fig. 3c).

Monocyte/macrophage markers were more discordant, with less than 50% of cells retaining phenotypic assignment between modalities (IMC 47% concordance, IF 41% concordance). Since macrophages have large, irregular membranes that often overlap with other cells, the phenotyping is more sensitive to differences in intensity thresholds, cell segmentation, and alignment. This issue is exacerbated in nucleus-based cell segmentation, which captures the morphology of small, round cells like lymphocytes better than large, irregular, or multinucleated cells. Overall, results on IMC were able to validate our findings in IF, and we found concordance between the two modalities high enough to allow for possible panel expansion using this method in the future.

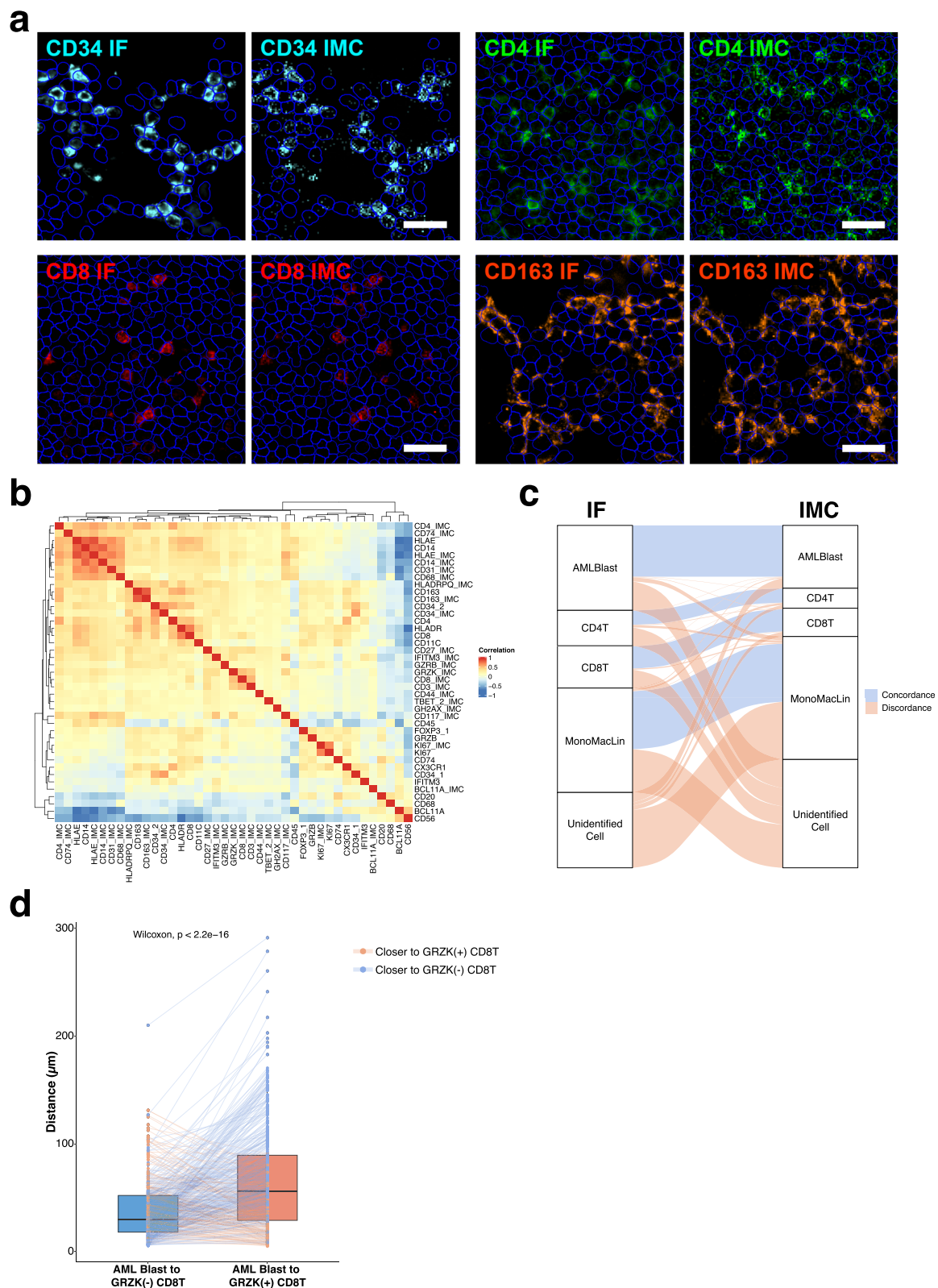


Fig. 3 | Spatial IF to IMC results in degradation of nuclear signal in IMC without compromising antigen signal. a Comparison of CD34 (pseudocolored cyan), CD4 (pseudocolored green), CD8 (pseudocolored red), and CD163 (pseudocolored orange) staining performance in IF and IMC shows high concordance, validating cell segmentation and spatial alignment approaches. Scale bar, 25 μm . **b** Correlation of

the same slide imaging between IF and IMC markers. **c** Alluvial plot showing proportions of concordance and discordance of the same cells phenotyped using only IMC markers and using only IF markers. **d** Distance of AML cells to granzyme K-negative and granzyme K-positive cells. Connected dots represent the distances for the same AML blast cell (paired Wilcoxon test, $p < 2.2e-16$).

With subsequent IMC staining, we were able to image additional markers without increasing COMET cycle count. We previously published that a subset of stem-like/memory CD8 T cells expressing granzyme K (GZMK) was enriched in responders to immunotherapy in AML¹⁸. We hypothesized that AML cells could have a spatial relationship with GZMK(+) CD8(+) T cells. Using the expanded panel provided by IMC, we found that CD34(+) AML cells were significantly closer to GZMK(-) CD8(+) T cells than GZMK(+) CD8 T(+) cells (Fig. 3d). This could possibly indicate an immune-evasive response to T cells with memory-like properties, which are more likely to trigger bystander activation in inflammatory environments¹⁹.

Spatial region analysis unveils tertiary lymphoid-like aggregates in adult AML

Recent developments in spatial neighborhood analysis have allowed for the identification of regions based on patterns of local cell proximity, identifying novel areas of interaction and structure with potential prognostic/therapeutic implications²⁰. To test this in AML, we applied unbiased clustering over Ripley's K function, a statistical measure of the spatial dispersion of each cell type modeled as a local point process. This revealed five distinct regions distinguished by different proportions of cell types, suggesting unique cell-cell interactions (Fig. 4a, b, Supplementary Fig. 5). Region_1 was highly enriched in AML blasts and significantly correlated to flow cytometry blast percentage ($R = 0.92$, $p = 3 \times 10^{-7}$) (Supplementary Fig. 6a). Region_2 was primarily enriched in lymphocytes and cells of monocyte and macrophage lineage. Region_3 had a high concentration of B cells, CD4(+) T cells, CD8(+) T cells, and NK cells. Region_4 was an even mix of cell types, and region_5 captured mainly unidentified cells.

Region_4 was the largest in area, as expected from the unstructured liquid formation of the BMM. Interestingly, region_3 only appeared in tumor cores of 3/7 patients (TMA7-3C, TMA8-3C, and TMA8-5E) and consisted of a tight cluster of B and T lymphocytes (Fig. 4c). These aggregates varied in size and organization, with TMA8-3C having the largest aggregate and rough organization of a B/CD4 T cell core and CD4/CD8 T cell border, while TMA8-3C and TMA8-5E were much smaller and contained a thoroughly mixed B and T cell population. This finding was consistent with various states of maturity of TLS found in solid tumors based on composition and organization. B cells in region_3 also displayed significantly higher expression of Ki67 than in region_2 ($p = 0.047$) and region_4 ($p = 1.46 \times 10^{-4}$), possibly indicative of a proliferative B-cell core, a previously reported characteristic of TLS in solid cancers (Supplementary Fig. 6b). We then stratified patients by presence of region_3 aggregates. Looking at differences between cell densities, we were surprised to find that patients with region_3 aggregates had significantly higher densities of monocyte and macrophage lineage cells ($p = 0.0164$), and while T and B cells were slightly higher in density, they were not significantly so (Fig. 5a). While overall densities were similar, patients with region_3 aggregates exhibited a significantly higher percentage of CD4(+) ($p = 0.017$) and CD8(+) T cells ($p = 0.041$) in the AML-enriched region_1, analogous to increased tumor lymphocyte infiltration in solid tumors (Fig. 5b). We then were able to validate the presence of these aggregates through the 7-color (Supplementary Table 5) Opal multiplex IF assay by staining subsequent sections of the original TMA blocks (Fig. 5c, Supplementary Fig. 6c). We also tested alternate methods for neighborhood detection and found similar results, with less specificity for region_3 likely due to focusing on local spatial patterns (Supplementary Figs. 7–9)^{8,20,21}. TLS presence in AML remains poorly studied, with most research focusing on solid tumors. Recently, a study has described these clusters of lymphocytes as “TLS-like aggregates” in a pediatric AML cohort²². As such, we chose to adapt this terminology to reflect the lack of conclusive definitions of TLS in AML. In summary, by clustering local measures of spatial association, we were able to spatially identify a cluster of cells, denoted by region_3, of lymphocyte aggregates that resemble various stages of TLS formation and maturity in AML. These aggregates were further validated by the Opal assay.

TLS signatures identified in Bulk RNA-seq and Spatial transcriptomics AML datasets are correlated with prognosis

Though we were able to discover TLS-like aggregates with the COMET, spatial proteomics is relatively low-plex compared to RNA-seq, and our panel excluded many functional TLS markers. Using 6 published gene signatures for TLS^{23–28} (Supplementary Table 6), we investigated the presence of TLS in AML using the Visium (10x Genomics, Pleasanton, CA) spatial transcriptomics platform, which can capture the transcriptome of the AML BMM at a resolution of 55 μm spots. We focused on the signature from Cabrita et al. as it is derived from a compendium of TLS-associated genes²³ and not cancer-specific. We performed the Visium assay on an archived bone marrow sample with a positive lymphocyte aggregate by H&E stain. Using the local Lee's L bivariate spatial statistic²⁹, we found highly concordant spatial enrichment of the TLS signature by Cabrita et al. with deconvolution signatures of T cells and B cells, further suggesting TLS-like properties for these lymphocyte aggregates in AML³⁰ (Fig. 6a).

We further investigated the presence of TLS in AML using a bulk RNA-seq dataset integrating data from TCGA³¹, MDACC³², and BEAT-AML1/2³³ datasets and found signatures published by Cabrita et al. and Hou et al. to be predictive of overall survival (Fig. 6b, c). Additionally, in the 3/4 of the datasets, all 6 signatures significantly correlated with HLA-E expression, which we previously identified as a marker for immune evasion in AML³⁴, and was significantly indicative of survival in the combined bulk RNA dataset (Supplementary Fig. 10a and Fig. 6d). The TLS signature also significantly correlated with hallmark scores for hypoxia, interferon-alpha (IFN- α) response, interferon-gamma (IFN- γ) response, inflammatory response, and angiogenesis in our AML dataset (Fig. 6e). When looking across the entire TCGA dataset, median TLS score for AML was relatively low (-0.45 , rank 24/32), suggesting rarer or subdued TLS signaling programs in AML (Supplementary Fig. 10b). Diffuse large B-cell lymphoma had the highest median TLS score (0.76), possibly due to aberrant *CCR7* expression in malignant B cells³⁵.

Discussion

Uncovering AML-BMM interactions is essential to untangling the complex interplay between leukemia and immunotherapy. Comprehensive characterization of the BMM is necessary to determine cell states and interactions, and requires targeting of tumor, immune, and structural components to uncover deeper spatial characteristics.

AML is a heterogeneous disease, with a diverse range of phenotypic markers that contain a high overlap with normal hematopoietic cells. Currently, no singular marker can confidently phenotype AML blast cells, and clinical diagnostic flow cytometry panels for AML exceed 20+ markers to differentiate AML immunophenotypes, which carry diagnostic and prognostic implications². Other groups have combined multiple targeted spatial imaging modalities for same slide imaging to improve cell segmentation or augment cell identification and analysis^{36–38}. We employed IMC to validate our findings in IF, with the additional benefit of expanding the panel size without subjecting the tissue to additional imaging cycles. By using an adjacent H&E-stained slide as reference, we can align to a minimally treated image that reduces tissue damage or bone detachment from antigen retrieval and multiple staining rounds³⁹. This is particularly important in cyclic imaging technologies, which require morphologic similarity at the micron level over multiple captures for accurate image registration, cell segmentation, and background subtraction⁴⁰. Furthermore, lack of autofluorescence in IMC makes it ideal for targeting cells with high lipofuscin or pigment⁴⁰, while high-resolution and lack of conjugation in COMET make it suitable for rapidly querying biomarkers of interest and interrogating subcellular expression⁶. Additionally, other structural stains relevant to bone marrow pathology, such as trichrome and silver stains, can be performed. Overall, our study finds sequential IF and IMC reliable methods for interrogating the BMM, with good concordance after alignment.

By clustering the spatial K function of each cell, we were able to reveal B and T cell aggregates that resembled various maturation states of TLS in solid tumors⁴¹. Current definitions of TLS are variable, and several

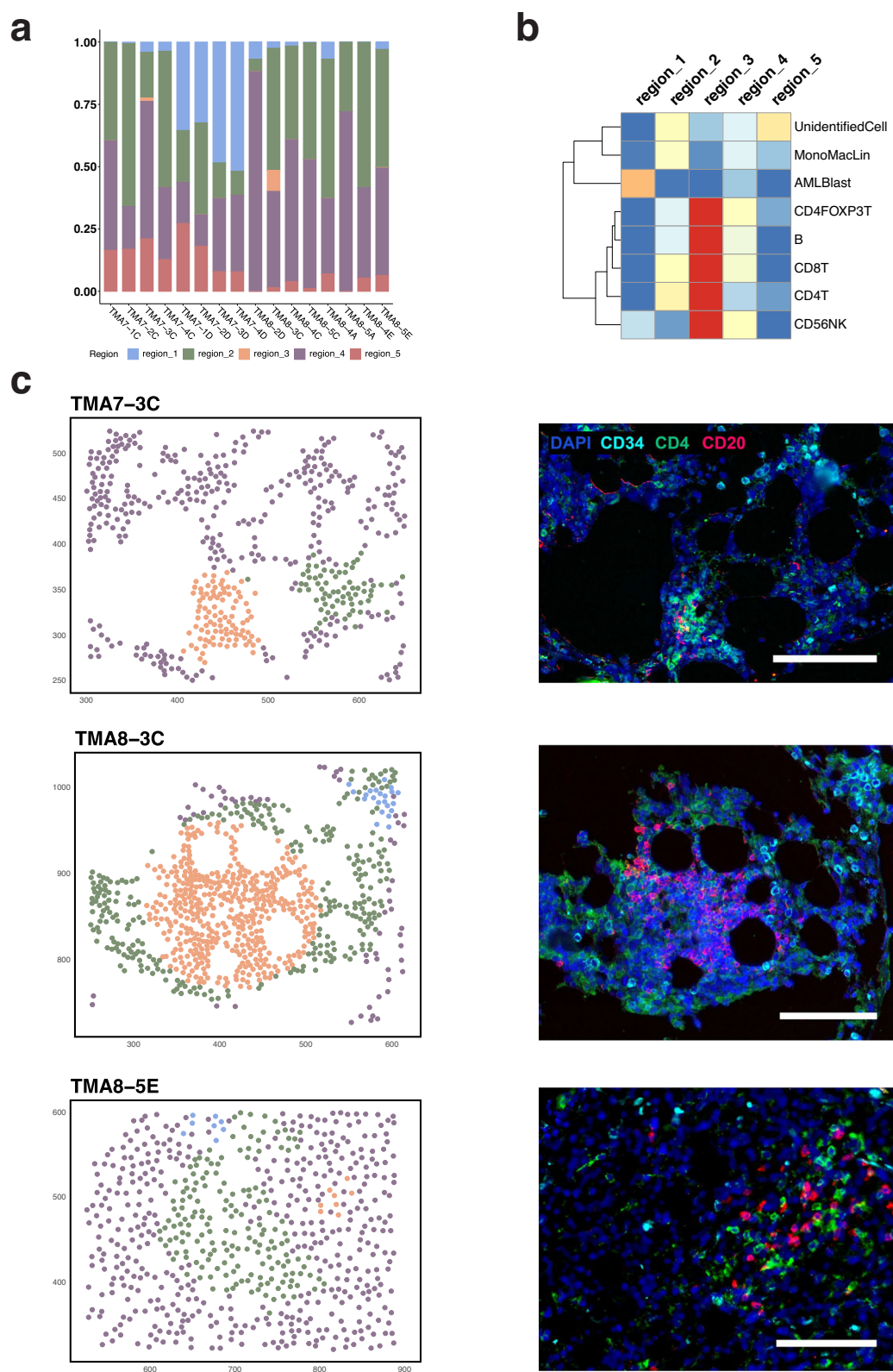


Fig. 4 | Spatial neighborhoods reveal tertiary lymphoid-like aggregates.
a Unbiased clustering of the spatial K function for each cell type reveals five different cellular regions of varying proportions per tissue core. Of note, region_3 only appears in three cores. **b** Relative enrichment of cell types for each cellular region. **c** Region assignment of cells within the TLS-like structures, with corresponding micrographs. CD34(+) AML cells are shown in pseudocolored cyan, CD4(+) T cells in pseudocolored green, and CD20(+) B cells in pseudocolored red. DAPI (pseudocolored blue) was used as a nuclear counterstain. Scale bar, 100 μ m.

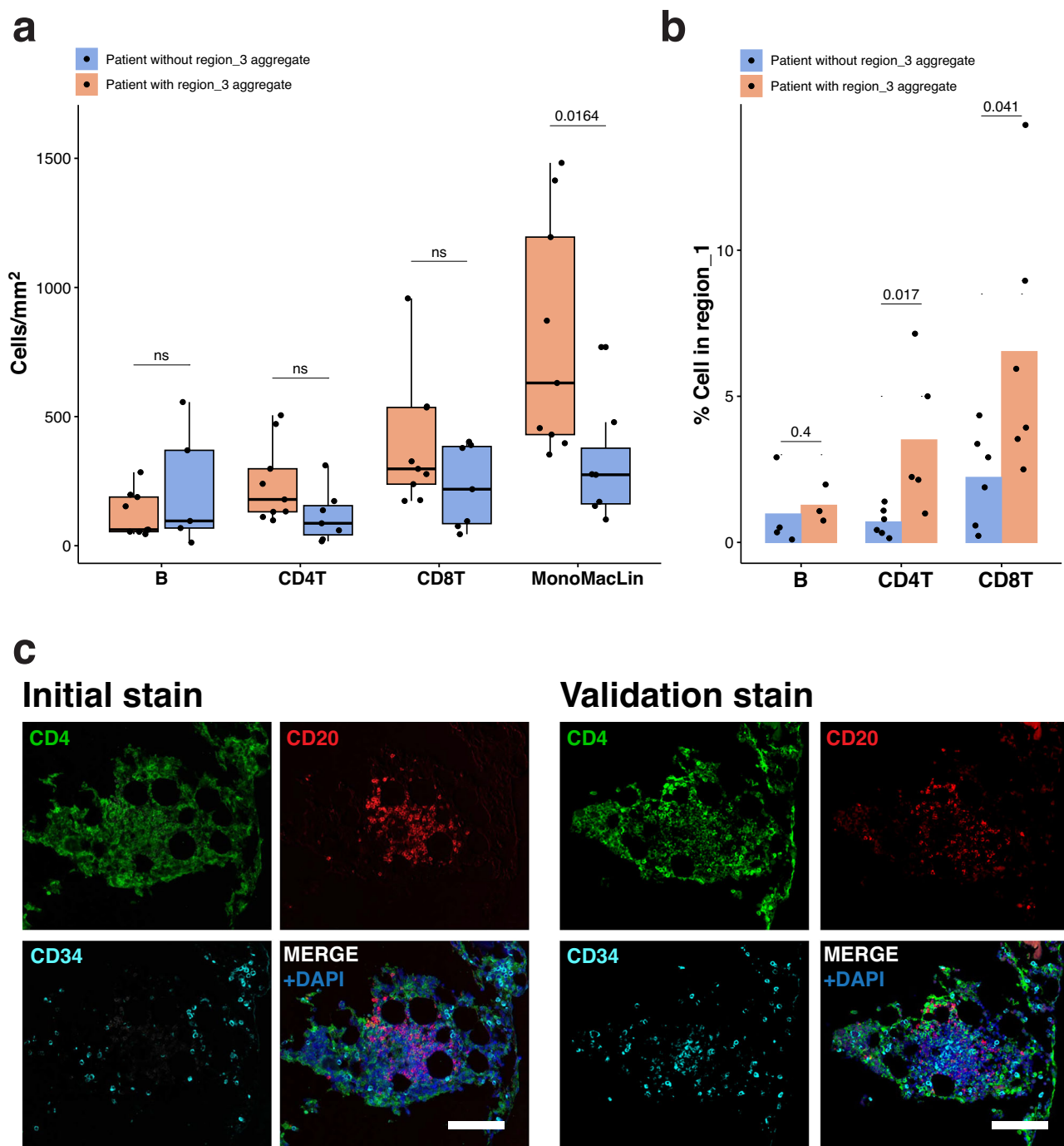


Fig. 5 | Spatial analysis reveals microenvironmental differences with lymphocyte aggregates. **a** Cell densities for B cells, CD4(+) T cells (CD4T), CD8(+) T cells (CD8T), and monocyte-macrophage lineage cells (MonoMacLin). Each dot represents an individual TMA core (Wilcoxon test). **b** Percent of B cells, CD8(+) T cells, and CD4(+) T cells in region_1 (AML-enriched) areas between TMA cores with and without region_3 aggregates. Dots represent an individual TMA core (Wilcoxon

test). **c** Micrographs showing COMET stain and Opal validation stain for the region_3 aggregate of TMA8-3C. The two methods showed similar staining patterns for CD4 (pseudocolored green), CD8 (pseudocolored red), and CD34 (pseudocolored cyan). DAPI (pseudocolored blue) was used as a nuclear counterstain. Scale bar, 100 μ m.

delineations of TLS maturity and development have been proposed, with the most immature state being a loose lymphocyte aggregate while the most mature feature an organized cluster of lymphocytes with a germinal center, high endothelial venules, T follicular helper cells, and follicular dendritic cells⁴¹. Lymphocyte aggregates have long been observed in bone marrow, being described on a spectrum from disorganized clusters to structures resembling classical TLS. Their effect on the AML BMM however has not been thoroughly detailed^{42,43}. These “TLS-like aggregates” were recently observed in a pediatric AML population and found to be increased in

number after immunotherapy²². Interestingly, all of the patients in our study exhibiting TLS-like aggregates ($n = 3$) were positive for *TP53* mutation, while their cohort was enriched for *KMT2A* rearrangement. Tumor protein p53 (TP53) is a well-known cancer driver that has been associated with TLS signatures in several cancers and corresponds with poor prognosis in AML^{44,45}. TLS is thought to be formed under chronic inflammatory conditions⁴⁶, and similarly, AML progression and pathogenesis have been linked to inflammation⁴⁷. Our previous work implicated HLA-E as an immune evasion reaction of AML cells upregulated in response to

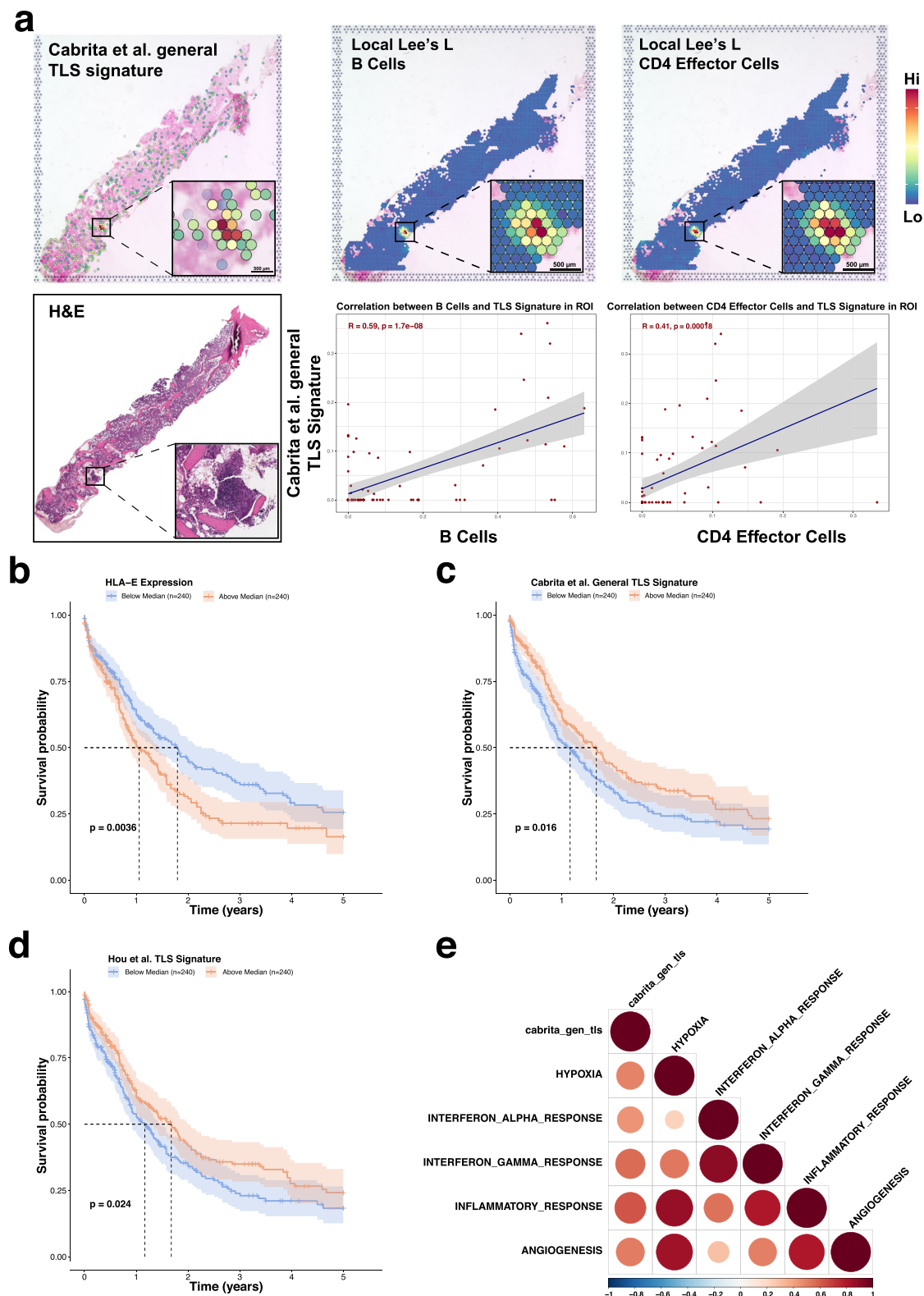


Fig. 6 | TLS signatures show prognostic value in transcriptomics. **a** Spatial transcriptomics of Cabrita et al. TLS signature shown with the Local Lee's L spatial statistic when using a B cell signature as a covariate, and when using a CD4 effector T cell signature as a covariate, along with the correlation between signatures in the TLS-like ROI (Pearson correlation test). **b** Kaplan–Meier survival curves of AML patients from TCGA, Beat-AML, and MDACC by median score of the Hou et al. TLS

signature. **c** Kaplan–Meier survival curves of AML patients from TCGA, Beat-AML, and MDACC by median score of the Cabrita et al. TLS signature. **d** Kaplan–Meier survival curves of AML patients from TCGA, Beat-AML, and MDACC by median HLA-E expression. **e** Correlation plot of Cabrita et al. TLS signature and significantly correlated Hallmark signatures (Pearson correlation test).

inflammatory cytokines such as IFN- γ ³⁴. This finding is corroborated by the strong correlation between HLA-E expression and a validated TLS score in a large, integrated public AML dataset. Our research shows that the transcriptomic signature of these TLS-like aggregates can be observed spatially and corresponds with better survival, similar to that of TLS in solid cancers^{25,48,49}. Though in the present study we lack the ability to detect features of mature TLS, our integration of multiple spatial proteomics, spatial transcriptomics, and bulk RNA assays suggests that the presence of bona-fide TLS may exist in AML.

Currently, many questions remain unanswered about the state of TLS-like and lymphocyte aggregates in AML. Lymphocyte aggregates in bone marrow are relatively rare in occurrence, estimated to be between 1 and 13%⁵⁰. Even more rare, Agbay et al. reported less than 0.02% incidence of reactive germinal centers in 205,274 bone marrow specimens, and none in the context of AML⁵¹. In contrast, TLS is reported to occur in up to 60% of breast cancer cases⁵². Several models of TLS maturation suggest lymphocyte aggregates as the initial steps to TLS formation^{41,53}. Though only three aggregates were found in the present study, only one had characteristics resembling a mature TLS. As previous studies have shown that only mature TLS exhibits favorable prognostic value^{44,48}, understanding mechanism of TLS formation and maturation in AML compared to other cancers is crucial. Currently, the value of inducing TLS remains uncertain. The stimulator of interferon genes (STING) agonist ADU S-100 has been reported to promote TLS formation through lymphotoxin- α (LT α), interleukin-36 beta (IL-36 β), and tumor necrosis factor- α (TNF- α) in a melanoma mouse model⁵⁴, however, clinical trials of STING agonists have had disappointing results⁵⁵ with companies halting development on STING agonists GSK3745417, MK-1454, and ADU-S-100. Additional areas of investigation include prognostic features of TLS, which include TLS maturity, TLS density, and intra- or peri-tumor location in solid tumors⁵⁶. Though not all these features are directly applicable to liquid malignancies, possible analogs in the AML BMM could include size, proximity, and density of TLS around AML-enriched spatial neighborhoods. Given the potential impact on immune response and scarcity of research on TLS in AML, further study into these TLS-like aggregates, their factors of formation and maturation, their interaction with the BMM, and their effect on immunotherapy is warranted.

In summary, we were able to characterize a TLS-like aggregate in AML patients through an optimized, flexible, and cost-effective pipeline performant enough to spatially interrogate the leukemic BMM at the single-cell level using the same slide IF and IMC. We were able to further validate the presence of TLS-like aggregates using established TLS signatures in spatial transcriptomics and public AML datasets and show correlations to prognostic impact. Further research into TLS-like aggregates in the BMM could help unveil spatial factors of durable immune response in AML.

Methods

TMA preparation

16 bone marrow biopsies from 7 patients were retrieved from the Department of Hematopathology archives at the University of Texas MD Anderson Cancer Center and organized into two tissue microarrays (TMAs). Patients gave informed consent for sample collection. The study protocol was approved by MD Anderson's Institutional Review Board and was conducted in accordance with the principles of the Declaration of Helsinki. Regions of interest (ROIs) for each sample were annotated using the TMA control software to select for focal areas of cellularity (3DHISTECH, Budapest, Hungary). A FFPE TMA block was created by embedding a 1.5-mm diameter circular core from each donor block with 0.5 mm spacing using the TMA Grand Master (3DHISTECH), which was sectioned at 4 μ m to create a series of TMA slides.

COMET multiplex IF

FFPE TMA slides underwent dewax and hydration largely as previously described⁵⁷. Slides then underwent HIER at 107 °C for 15 minutes. For testing of the Lunaphore protocol, dewax and antigen retrieval were

performed using the PT module (Epredia, Kalamazoo, MI) as previously described⁶. For testing of the TrueBlack, TrueBlack lipofuscin autofluorescence quencher (Biotium, Fremont, CA) was applied according to manufacturer directions. The slide was then loaded into the COMET to fit in the 9×9 mm square imaging window. Staining, imaging, and elution were performed largely as previously described⁶. Primary antibodies and dilutions are found in Supplementary Table 1. Imaged slides were stored in PBS at 4 °C until ready to stain for IMC.

Opal multiplex IF

FFPE TMA slides from the same blocks were baked, dewaxed, and treated with 3% peroxide. Tissue then underwent the 7-color Opal multiplex staining workflow. In short, slides underwent HIER, blocked, and incubated with primary antibodies. Slides were then incubated with horseradish peroxidase, then Opal fluorophores, stripping out the antibodies between each marker before counterstaining with DAPI and mounting with a coverslip. All steps were performed on the NanoVIP 100 automated stainer (BioGenex, Fremont, CA). Slides were then imaged at ×40 using the PhenoImager HT 2.0 (Akoya Biosciences, Marlborough, MA).

IMC staining and imaging

Briefly, the TMA slide was treated with blocking buffer and permeabilization reagents, incubated in a cocktail of metal-conjugated antibodies, and counter-stained with iridium intercalator (201192B; Standard BioTools, San Francisco, CA). After drying, ROIs were drawn to select COMET-imaged cores, which were imaged at ×10 using the Hyperion XTi (Standard BioTools). The resulting MCD files were converted into TIFF by MCD Viewer (v1.0.560.6; Standard BioTools).

Image analysis

Image files were analyzed using the Visiopharm image analysis software (v2023.09; Visiopharm, Hoersholm, Denmark). COMET IF, IMC, and H&E images were aligned using the TissueAlign function guided by major tissue landmarks and coexpression of markers across assays. Detection of hematopoietic tissue and bone tissue was performed using a random forest classifier on the DAPI stain and the H&E stain, respectively. Areas with necrosis, crushed cells, poor focus, misaligned stitching, or high autofluorescence were removed. COMET image background subtraction was performed by subtracting the autofluorescence captures scaled by the average autofluorescence of previous runs per channel from the marker image. Cell segmentation was achieved by detecting cell nuclei using DAPI or iridium counterstains with a deep learning algorithm pre-trained on a U-Net convolutional neural network. Cells were classified using a supervised gating strategy based on mean intensity thresholds applied to canonical markers, while leukemic blasts were annotated using patient-specific immunophenotypes obtained by flow cytometry. For validation using the Opal staining workflow, cores with lymphocyte aggregates in the COMET assay were selected for comparison of staining. Cell labels, mean fluorescence intensities, and XY positions were exported.

Visium

Briefly, FFPE bone marrow samples were processed using the standard CytAssist protocol from 10x Genomics. SpaceRanger (v2.0) was used to align sequences to the reference genome and to map spots to the tissue. Spots were filtered by median absolute deviation, normalized using SCTransform(), and variable genes were identified using FindVariableFeatures() in Seurat⁵⁸. Cell deconvolution used the Seurat transfer learning pipeline, leveraging in-house single-cell RNA-seq data. TLS signatures were scored using the AUCell R package⁵⁹. Local Lee's L was computed by adapting methods from the Voyager R package³⁰. All software used is listed in Supplementary Table 7.

Bulk data

RNA-seq data and corresponding clinical data from TCGA, Beat-AML, and MDACC were downloaded and integrated into one dataset. Batch effects were corrected using ComBat-seq⁶⁰. TLS signatures obtained from the literature were used to score the data using the R package GSVA⁶¹.

Statistical analysis

All statistical analyses were performed in the R statistical software (v4.3.0) using the rstatix R package. Marker expression was arcsinh-transformed, batch-corrected with Harmony⁶², and analyzed using the imcRtools package⁶³. Spatial regions were generated with the lisaClust package⁶⁴. Cell distances were calculated using the minDistToCells() function. A two-sided Wilcoxon rank sum test was used for comparisons between two independent groups, while the paired Wilcoxon test was used for paired data. Survival curves were created using the Kaplan–Meier method and assessed using the log-rank test. Pearson’s correlation was used for all correlative tests. All statistical tests used an alpha of 0.05.

Data visualization

The pipeline workflow was created in BioRender (BioRender, Toronto, Canada). Figures were constructed using the ComplexHeatmap⁶⁵, pheatmap, ggplot2, ggpubr, and dittoSeq⁶⁶ R packages and composed in Illustrator (v28.1; Adobe, San Jose, CA). All boxplots use median for the center line. Micrographs were created by cropping original image files, then layering and applying pseudocolor in Photoshop (v25.5.1; Adobe) through linear mapping. Whole image brightness adjustments (levels) were made for visibility.

Data availability

Captured primary COMET images are available at <https://doi.org/10.6084/m9.figshare.28861841> in addition to an interactive viewer⁶⁷. The following public datasets were used in this publication and can be accessed at their respective locations: BEAT-AML (<https://www.nature.com/articles/s41586-018-0623-z#Sec38>), TCGA (<https://gdc.cancer.gov/about-data/publications/pancanatlas>), MD Anderson (GEO accession GSE165656).

Code availability

The underlying code for this study is available on GitHub and can be accessed via <http://github.com/abbaslab/>.

Received: 26 June 2024; Accepted: 21 March 2025;

Published online: 20 May 2025

References

- Longo, D. L., Döhner, H., Weisdorf, D. J. & Bloomfield, C. D. Acute myeloid leukemia. *N. Engl. J. Med.* **373**, 1136–1152 (2015).
- Döhner, H. et al. Diagnosis and management of acute myeloid leukemia in adults: recommendations from an international expert panel, on behalf of the European LeukemiaNet. *Blood* **115**, 453–474 (2010).
- Daver, N. et al. Azacitidine (AZA) with nivolumab (Nivo), and AZA with Nivo +Ipilimumab (Ipi) in relapsed/refractory (R/R) acute myeloid leukemia: clinical and immune biomarkers of response. *Blood* **136**, 43–45 (2020).
- Tettamanti, S., Pievani, A., Biondi, A., Dotti, G. & Serafini, M. Catch me if you can: how AML and its niche escape immunotherapy. *Leukemia* **36**, 13–22 (2022).
- Colmone, A. et al. Leukemic cells create bone marrow niches that disrupt the behavior of normal hematopoietic progenitor cells. *Science* **322**, 1861–1865 (2008).
- Rivest, F. et al. Fully automated sequential immunofluorescence (seqIF) for hyperplex spatial proteomics. *Sci. Rep.* **13**, 16994 (2023).
- Giesen, C. et al. Highly multiplexed imaging of tumor tissues with subcellular resolution by mass cytometry. *Nat. Methods* **11**, 417–422 (2014).
- Goltsev, Y. et al. Deep profiling of mouse splenic architecture with CODEX multiplexed imaging. *Cell* **174**, 968–981.e15 (2018).
- Wählby, C., Erlandsson, F., Bengtsson, E. & Zetterberg, A. Sequential immunofluorescence staining and image analysis for detection of large numbers of antigens in individual cell nuclei. *Cytometry* **47**, 32–41 (2002).
- Vanhersecke, L. et al. Mature tertiary lymphoid structures predict immune checkpoint inhibitor efficacy in solid tumors independently of PD-L1 expression. *Nat. Cancer* **2**, 794–802 (2021).
- Zhu, G. et al. Induction of tertiary lymphoid structures with antitumor function by a lymph node-derived stromal cell line. *Front. Immunol.* **9**, 1609 (2018).
- Gruchy, J. R., Barnes, P. J. & Haché, K. A. D. CytoLyt® fixation and decalcification pretreatments alter antigenicity in normal tissues compared with standard formalin fixation. *Appl. Immunohistochem. Mol. Morphol.* **23**, 297–302 (2015).
- Lara, O. D. et al. Tumor core biopsies adequately represent immune microenvironment of high-grade serous carcinoma. *Sci. Rep.* **9**, 17589 (2019).
- Jarosch, S. et al. Multiplexed imaging and automated signal quantification in formalin-fixed paraffin-embedded tissues by ChipCytometry. *Cell Rep. Methods* **1**, 100104 (2021).
- Prentice, A. I. D. Autofluorescence of bone tissues. *J. Clin. Pathol.* **20**, 717 (1967).
- Monici, M. Cell and tissue autofluorescence research and diagnostic applications. *Biotechnol. Annu. Rev.* **11**, 227–256 (2005).
- Baer, M. R. et al. Expression of the neural cell adhesion molecule CD56 is associated with short remission duration and survival in acute myeloid leukemia with t(8;21)(q22;q22). *Blood* **90**, 1643–1648 (1997).
- Abbas, H. A. et al. Single cell T cell landscape and T cell receptor repertoire profiling of AML in context of PD-1 blockade therapy. *Nat. Commun.* **12**, 6071 (2021).
- Whiteside, S. K., Snook, J. P., Williams, M. A. & Weis, J. J. Bystander T cells: a balancing act of friends and foes. *Trends Immunol.* **39**, 1021–1035 (2018).
- Schürch, C. M. et al. Coordinated cellular neighborhoods orchestrate antitumoral immunity at the colorectal cancer invasive front. *Cell* **182**, 1341–1359.e19 (2020).
- Nirmal, A. J. & Sorger, P. K. SCIMAP: a python toolkit for integrated spatial analysis of multiplexed imaging Data. *J. Open Source Softw.* **9**, 6604 (2024).
- Koedijk, J. B. et al. Spatial analysis reveals distinct immune phenotypes and tertiary lymphoid structure-like aggregates in pediatric acute myeloid leukemia. *Leukemia* **38**, 2332–2343 (2023).
- Dieu-Nosjean, M.-C., Goc, J., Giraldo, N. A., Sautès-Fridman, C. & Fridman, W. H. Tertiary lymphoid structures in cancer and beyond. *Trends Immunol.* **35**, 571–580 (2014).
- Cabrita, R. et al. Tertiary lymphoid structures improve immunotherapy and survival in melanoma. *Nature* **577**, 561–565 (2020).
- Gu-Trantien, C. et al. CD4+ follicular helper T cell infiltration predicts breast cancer survival. *J. Clin. Invest.* **123**, 2873–2892 (2013).
- Hou, Y. et al. The gene signature of tertiary lymphoid structures within ovarian cancer predicts the prognosis and immunotherapy benefit. *Front. Genet.* **13**, 1090640 (2023).
- Coppola, D. et al. Unique ectopic lymph node-like structures present in human primary colorectal carcinoma are identified by immune gene array profiling. *Am. J. Pathol.* **179**, 37–45 (2011).
- Wang, Q. et al. Tertiary lymphoid structures predict survival and response to neoadjuvant therapy in locally advanced rectal cancer. *npj Precis. Oncol.* **8**, 61 (2024).
- Lee, S.-I. Developing a bivariate spatial association measure: an integration of Pearson’s r and Moran’s I. *J. Geogr. Syst.* **3**, 369–385 (2001).
- Moses, L. et al. Voyager: exploratory single-cell genomics data analysis with geospatial statistics. *bioRxiv* <https://doi.org/10.1101/2023.07.20.549945> (2023).
- Network, C. G. A. R. et al. Genomic and epigenomic landscapes of adult de novo acute myeloid leukemia. *N. Engl. J. Med.* **368**, 2059–2074 (2013).
- Abbas, H. A. et al. Decoupling lineage-associated genes in acute myeloid leukemia reveals inflammatory and metabolic signatures associated with outcomes. *Front. Oncol.* **11**, 705627 (2021).
- Tyner, J. W. et al. Functional genomic landscape of acute myeloid leukaemia. *Nature* **562**, 526–531 (2018).

34. Wang, B. et al. Comprehensive characterization of IFN γ signaling in acute myeloid leukemia reveals prognostic and therapeutic strategies. *Nat. Commun.* **15**, 1821 (2024).
35. Uhl, B. et al. Distinct chemokine receptor expression profiles in de novo DLBCL, transformed follicular lymphoma, Richter's Transformed DLBCL and germinal center B-cells. *Int. J. Mol. Sci.* **23**, 7874 (2022).
36. Baars, M. J. D. et al. MATISSE: a method for improved single cell segmentation in imaging mass cytometry. *BMC Biol.* **19**, 99 (2021).
37. Marlin, M. C. et al. A novel process for H&E, immunofluorescence, and imaging mass cytometry on a single slide with a concise analytics pipeline. *Cytom. Part A* **103**, 1010–1018 (2023).
38. Lin, J.-R. et al. High-plex immunofluorescence imaging and traditional histology of the same tissue section for discovering image-based biomarkers. *Nat. Cancer* **4**, 1036–1052 (2023).
39. Harms, P. W. et al. Multiplex immunohistochemistry and immunofluorescence: a practical update for pathologists. *Mod. Pathol.* **36**, 100197 (2023).
40. Kim, E. N. et al. Dual-modality imaging of immunofluorescence and imaging mass cytometry for whole-slide imaging and accurate segmentation. *Cell Rep. Methods* **3**, 100595 (2023).
41. Chen, Y., Wu, Y., Yan, G. & Zhang, G. Tertiary lymphoid structures in cancer: maturation and induction. *Front. Immunol.* **15**, 1369626 (2024).
42. Naemi, K. et al. Benign lymphoid aggregates in the bone marrow: distribution patterns of B and T lymphocytes. *Hum. Pathol.* **44**, 512–520 (2013).
43. Bao, Q., Zhang, Z., Shen, Y. & Zhang, W. 409P Tertiary lymphoid structures are scarce but associated with BCR clonal expansion, B cell activity and checkpoint inhibitor response in advanced osteosarcoma. *Ann. Oncol.* **33**, S1602 (2022).
44. Domblides, C. et al. Tumor-associated tertiary lymphoid structures: from basic and clinical knowledge to therapeutic manipulation. *Front. Immunol.* **12**, 698604 (2021).
45. Lin, Z. et al. Pan-cancer analysis of genomic properties and clinical outcome associated with tumor tertiary lymphoid structure. *Sci. Rep.* **10**, 21530 (2020).
46. Antonioli, L. et al. Ectopic lymphoid organs and immune-mediated diseases: molecular basis for pharmacological approaches. *Trends Mol. Med.* **26**, 1021–1033 (2020).
47. Kristinsson, S. Y. et al. Chronic immune stimulation might act as a trigger for the development of acute myeloid leukemia or myelodysplastic syndromes. *J. Clin. Oncol.* **29**, 2897–2903 (2011).
48. Gan, X. et al. Spatial multimodal analysis revealed tertiary lymphoid structures as a risk stratification indicator in combined hepatocellular-cholangiocarcinoma. *Cancer Lett.* **581**, 216513 (2024).
49. Horeweg, N. et al. Tertiary lymphoid structures critical for prognosis in endometrial cancer patients. *Nat. Commun.* **13**, 1373 (2022).
50. Maccio, U. & Rets, A. V. Lymphoid aggregates in bone marrow: a diagnostic pitfall. *J. Clin. Pathol.* **75**, 807–814 (2022).
51. Agbay, R. L. M. C. et al. Characteristics and clinical implications of reactive germinal centers in the bone marrow. *Hum. Pathol.* **68**, 7–21 (2017).
52. Narvaez, D. et al. The emerging role of tertiary lymphoid structures in breast cancer: a narrative review. *Cancers* **16**, 396 (2024).
53. Li, R. et al. Tertiary lymphoid structures favor outcome in resected esophageal squamous cell carcinoma. *J. Pathol.: Clin. Res.* **8**, 422–435 (2022).
54. Chelvanambi, M., Fecek, R. J., Taylor, J. L. & Storkus, W. J. STING agonist-based treatment promotes vascular normalization and tertiary lymphoid structure formation in the therapeutic melanoma microenvironment. *J. Immunother. Cancer* **9**, e001906 (2021).
55. Meric-Bernstam, F. et al. Combination of the STING agonist MIW815 (ADU-S100) and PD-1 inhibitor spartalizumab in advanced/metastatic solid tumors or lymphomas: an open-label, multicenter, phase Ib study. *Clin. Cancer Res.* **29**, 110–121 (2022).
56. Hayashi, Y. et al. Density and maturity of peritumoral tertiary lymphoid structures in oesophageal squamous cell carcinoma predicts patient survival and response to immune checkpoint inhibitors. *Br. J. Cancer* **128**, 2175–2185 (2023).
57. Ramos-Vara, J. A. Principles and methods of immunohistochemistry. In *Drug Safety Evaluation Methods and Protocols* (ed. Gautier, J.-C.) 1641 115–128 (Humana, New York, NY, 2017).
58. Satija, R., Farrell, J. A., Gennert, D., Schier, A. F. & Regev, A. Spatial reconstruction of single-cell gene expression data. *Nat. Biotechnol.* **33**, 495–502 (2015).
59. Aibar, S. et al. SCENIC: single-cell regulatory network inference and clustering. *Nat. Methods* **14**, 1083–1086 (2016).
60. Zhang, Y., Parmigiani, G. & Johnson, W. E. ComBat-seq: batch effect adjustment for RNA-seq count data. *NAR Genom. Bioinform.* **2**, lqaa078 (2020).
61. Hänzelmann, S., Castelo, R. & Guinney, J. GSVA: gene set variation analysis for microarray and RNA-Seq data. *BMC Bioinformatics* **14**, 7–7 (2013).
62. Korsunsky, I. et al. Fast, sensitive and accurate integration of single-cell data with Harmony. *Nat. Methods* **16**, 1289–1296 (2019).
63. Windhager, J. et al. An end-to-end workflow for multiplexed image processing and analysis. *Nat. Protoc.* **18**, 3565–3613 (2023).
64. Patrick, E. et al. Spatial analysis for highly multiplexed imaging data to identify tissue microenvironments. *Cytom. Part A* **103**, 593–599 (2023).
65. Gu, Z., Eils, R. & Schlesner, M. Complex heatmaps reveal patterns and correlations in multidimensional genomic data. *Bioinformatics* **32**, 2847–2849 (2016).
66. Bunis, D. G., Andrews, J., Fragiadakis, G. K., Burt, T. D. & Sirota, M. dittoSeq: universal user-friendly single-cell and bulk RNA sequencing visualization toolkit. *Bioinformatics* **36**, 5535–5536 (2020).
67. Hoffer, J. et al. Minerva: a light-weight, narrative image browser for multiplexed tissue images. *J. Open Source Softw.* **5**, 2579 (2020).
68. Khoury, J. D. et al. The 5th edition of the World Health Organization Classification of haematolymphoid tumours: myeloid and histiocytic/dendritic neoplasms. *Leukemia* **36**, 1703–1719 (2022).

Acknowledgements

We would like to thank Thomas Huynh and Arizona Nguyen at the Department of Veterinary Services at MD Anderson for their work and consultation on TMA design. H.A.A. was supported by a Physician Scientist Award. The work was partially funded by Cancer Prevention and Research Institute of Texas (CPRIT) Individual Investigator Research funding to H.A.A., philanthropic funding to H.A.A. and M.G. from Energy Transfer, and a philanthropic donation to H.A.A. from the Diego-Osio Llerenas Fund. This research was conducted in part at the Flow Cytometry & Cellular Imaging Core Facility and the Research Animal Support Facility, supported by the National Institutes of Health (NCI) through MD Anderson Cancer Center's Support Grant (P30 CA016672). Additional funding was provided by the NCI Research Specialist Award (R50 CA243707-01A1) and the Cancer Prevention and Research Institute of Texas (CPRIT) Shared Instrumentation Award (RP121010).

Author contributions

H.A.A. devised and directed the project; C.P.L. and I.V. co-analyzed the data. E.D. performed the spatial transcriptomics analysis. C.P.L. wrote the manuscript with contributions from H.A.A., I.V., S.F.B., P.K.R., and J.K.B.; A.V.B. and J.A.G. assisted in the acquisition and optimization of IMC and IF imaging; J.L.R. performed IMC antibody conjugation; C.P.L. performed the image analysis and quality check with assistance from C.D.P. and I.V.; F.Z.J. and A.E.Q. assisted in panel design and sample collection with C.B.R., T.M., B.C., and M.G.; S.J., S.B., and P.S. provided assistance in preparation and

analysis of the Visium assay. All authors provided feedback and contributed to the final manuscript.

Competing interests

All authors declare no competing interests.

Additional information

Supplementary information The online version contains supplementary material available at <https://doi.org/10.1038/s41698-025-00897-7>.

Correspondence and requests for materials should be addressed to Jared K. Burks or Hussein A. Abbas.

Reprints and permissions information is available at <http://www.nature.com/reprints>

Publisher's note Springer Nature remains neutral with regard to jurisdictional claims in published maps and institutional affiliations.

Open Access This article is licensed under a Creative Commons Attribution-NonCommercial-NoDerivatives 4.0 International License, which permits any non-commercial use, sharing, distribution and reproduction in any medium or format, as long as you give appropriate credit to the original author(s) and the source, provide a link to the Creative Commons licence, and indicate if you modified the licensed material. You do not have permission under this licence to share adapted material derived from this article or parts of it. The images or other third party material in this article are included in the article's Creative Commons licence, unless indicated otherwise in a credit line to the material. If material is not included in the article's Creative Commons licence and your intended use is not permitted by statutory regulation or exceeds the permitted use, you will need to obtain permission directly from the copyright holder. To view a copy of this licence, visit <http://creativecommons.org/licenses/by-nc-nd/4.0/>.

© The Author(s) 2025